RSC Applied Polymers

ROYAL SOCIETY OF CHEMISTRY

PAPER

View Article Online
View Journal | View Issue

Cite this: *RSC Appl. Polym.*, 2023, **1**, 73

Influence of post-processing on the properties of 3D-printed poly(propylene fumarate) star polymer hydroxyapatite nanocomposites†

Taylor R. Klein,‡[a] Alina Kirillova, ‡[a] Ken Gall[a,b] and Matthew L. Becker *[a,b,c]

Received 22nd April 2023,
Accepted 19th May 2023

DOI: 10.1039/d3lp00013c

rsc.li/rscapplpolym

Vat photopolymerization is able to produce intricate parts at high print speed, good part fidelity, and strong mechanical properties. However, as materials become more complex and printing technologies advance, the post-printing processing conditions of these parts must be considered. Poly(propylene fumarate) (PPF) 4-arm stars with a of degree of polymerization (DP) of 120 were photochemically 3D printed with 5 wt% hydroxyapatite (HAp) nanoparticles (<200 nm) as a filler in a nanocomposite scaffold targeted for bone regeneration applications. Nanocomposites and pure polymers were subjected to a number of post-printing processing conditions including UV post-curing times, cure temperatures and drying times in a vacuum oven. The impact of these conditions on mechanical properties were analyzed in compression, tension, and dynamic mechanical analysis (DMA). Mechanical behavior is highly tunable with the variation of each of these different processing conditions.

Introduction

In recent years, the advancement of 3D printing has brought new technologies to the world of medical devices and tissue engineering scaffolds, among others. 3D printing processes enable the production of complex structures and reduce material waste *versus* the traditional manufacturing approaches. One of these methods, vat photopolymerization, utilizes a light source to selectively crosslink a photocurable resin into the desired architecture.[1] Digital light processing (DLP) and continuous liquid interface production (CLIP), in particular, are methods that are able to produce strong, complex parts with high print fidelity at relatively high throughputs.[1] However, as the field of 3D printing grows in interest, there is a constant demand for the development of new printing technology and printable materials across fields.

The synthesis and subsequent fabrication of biodegradable materials is of particular interest, particularly the medical device industry. Polymers such as polylactic acid (PLA), polycaprolactone (PCL), and polyglycolic acid (PGA) have dominated this space.[2] Within the vat photopolymerization methods, acrylate monomers and acrylate-functionalized polymers remain the gold standard, owing to fast reaction rates and stability.[1,3] However, this stability resulting from carbon–carbon bonds produced in the 3D printing process inherently limits the potential for degradation of the printed construct. Poly(propylene fumarate) is a biodegradable polyester which is easily photochemically 3D printable *via* the alkene bond in its backbone.[2,4] It has been previously investigated for a variety of applications using SLA, DLP, and CLIP techniques to fabricate the respective constructs. PPF is easy to modify architecturally, with a collection from blocks to stars[5–7] to gradient copolymers. Star PPF has been shown to have a lower viscosity at higher molecular weights than linear PPF,[5] and it has been printed using a rapid thiol–ene reaction which increases degradability and enables a high degree of mechanical tunability within a biologically relevant regime.[7]

Integrating particles or fibers into a polymer matrix enables the formulation of a polymer composite. Traditionally fabricated using molding or casting, polymer composites possess enhanced mechanical performance or additional functionality when compared to the unaltered polymer alone.[8] Combining 3D printing and novel polymer composite materials is promising for the fabrication of complex parts with highly functional and tunable properties and performance. Polymer composites can be produced for a variety of target applications in augmenting the matrix polymer's properties in a multitude of ways. Bioactive ceramics such as hydroxyapatite (HAp),

[a]*Thomas Lord Department of Mechanical Engineering and Materials Science, Duke University, Durham, NC 27708, USA. E-mail: matthew.l.becker@duke.edu*
[b]*Department of Biomedical Engineering, Department of Orthopaedic Surgery, Duke University, Durham, NC 27708, USA*
[c]*Department of Chemistry, Duke University, Durham, NC 27708, USA*
†Electronic supplementary information (ESI) available: Characterization of composition, molecular mass and mechanical properties of the polymers and composite materials. See DOI: https://doi.org/10.1039/d3lp00013c
‡These authors contributed equally.

calcium phosphates, and bioactive glass can be used to improve cell adhesion and viability and promote cell differentiation in 3D-printed tissue engineered scaffolds,[9–13] while growth factors can also be incorporated into the polymer in order to enhance bioactive behavior.[11] Carbon nanotubes and graphene offer mechanical enhancement as well as improved electrical and thermal properties.[11] Additionally, certain nanoparticles have been utilized for strain sensors, piezoelectric composites, and magnetic-sensitive materials.[11,14]

In tissue engineering, hydroxyapatite (HAp) is a commonly used filler that is the primary inorganic constituent of bone and teeth[15] and is commonly used for bone defect repair and bone tissue engineering.[15,16] Hydroxyapatite is frequently manufactured through selective laser sintering methods to bind the ceramic powder together into the desired product shape,[15] but it has also previously been used some in DLP printing to produce scaffolds. However in most cases, rather than acting as a true composite, the ceramic constitutes a large volume fraction of the resin which is in turn printed into a structure, and the polymer in these cases acts as a binder and is removed in a sintering process which leaves only the ceramic behind.[15–17]

Microfillers and nanofillers can be added to a photopolymer resin for mechanical enhancement, additional functionality, and reduced part shrinkage.[11,18] However, fillers affect the printing of the photopolymer, and this effect should be considered. As light penetration is critical to the curing of the polymer, fillers must not contribute significantly to light scattering and still must enable cure depth into the resin.[19] Further, reducing viscosity is a crucial part of vat photopolymerization. The effect of fillers on the resin's viscosity must be minimized.[11] Nanoparticles have high surface-to-volume ratios which results in property enhancement at low loading, which would not increase the viscosity too much, and are small enough to not affect the layer height during layer-by-layer printing.[11,20] Vat photopolymerization methods also require post-processing and curing to complete the chemical reaction fully following the initial print. Steps to maximize properties using post-processing conditions can include heat, post-cure irradiation as well as printing conditions such as layer thickness and layer curing time for vat photopolymerization techniques.[21–23] However, there is little research investigating DLP 3D printing with nanofillers and how ideal post-processing conditions are influenced by the incorporation of these nanofillers.[24]

In this work, a previously explored UV-curable and bioresorbable PPF star polymer resin[7] has been augmented with a nanofiller of hydroxyapatite, and composite structures, including porous gyroid scaffolds, were 3D printed. Previous investigations of the unaltered resin and the nanocomposite resin have demonstrated the need for optimization and exploration of the post-processing curing conditions and their respective effects on the printed part. In the effort to maximize mechanical behavior, various post-printing processing conditions and their influence on the tensile and compression behavior of the printed structures with and without HAp were explored, such as post-curing time under UV, vacuum oven temperature during drying, and vacuum oven time. As a result, specific conditions were pinpointed that led to the maximized mechanical performance of the printed structures both under tensile and compression loading.

Experimental section

Materials

All reagents were purchased from Sigma-Aldrich and were used as received, unless otherwise noted. Solvents were purchased from Fisher Scientific and dried using a Pure Solv MD-3 solvent purification system. $Mg(BHT)_2(THF)_2$, was synthesized using methods described previously.[25] Propylene oxide was dried over calcium hydride overnight prior to distillation. *meso*-Erythritol was dried overnight under vacuum prior to use.

Methods

Synthesis of four-arm poly(propylene fumarate) stars. Four-arm star poly(propylene maleate) (PPM) was synthesized using methods described previously.[5–7] The ring opening copolymerization of maleic anhydride (MAn) and propylene oxide (PO) was initiated by *meso*-erythritol in toluene at 80 °C. $Mg(BHT)_2(THF)_2$ was used as a catalyst under an N_2 environment using standard Schlenk line techniques. A molar ratio of MAn : PO : initiator : catalyst = 150 : 150 : 1 : 0.4 was used. A degree of polymerization (DP_n) of 120 was targeted (30 repeat units for each of the four arms) by approaching 80% conversion of the reactants. Four-arm star PPM was then isomerized to PPF using 0.15 M equivalents of diethylamine in chloroform at 60 °C. The resulting product was washed three times with an aqueous 1 M sodium phosphate solution and subjected to rotary evaporation to remove excess solvent. Yield: ~350 g. SEC: M_w = 6.9 kDa M_n = 4.1 kDa, $Đ_M$ = 1.65. T_g = 9.3 ± 4.8 °C.[7]

Nuclear magnetic resonance (NMR) spectroscopy. Proton (^1H) NMR spectra were recorded using a Bruker AVANCE NEO 500 MHz spectrometer. Chemical shifts were recorded in parts per million (ppm) relative to the chloroform ($CDCl_3$) reference peak at δ = 7.26.

Size-exclusion chromatography (SEC). The number-average (M_n) and weight-average (M_w) molecular masses and molecular mass distributions were determined by SEC using an HLC-8420 GPC (Tosoh Bioscience). Molecular masses were calculated using a calibration curve generated from polystyrene standards with tetrahydrofuran (THF) as the eluent flowing at 0.5 mL min^{-1} and a sample concentration of 10.0 mg mL^{-1}.

Resin preparation. Resins for printing were prepared by diluting star-shaped PPF in ethyl acetate at a 60 : 40 (wt%) PPF : solvent ratio and the solutions were mixed on a rotating shaker. Defined mixtures of a thiol crosslinking agent, trimethylolpropane tris(3-mercaptopropionate) were investigated with a molar ratio of 10 : 1 (alkene : thiol). The formulation for printing consists of a photoinitiator, phenylbis(2,4,6-trimethylbenzoyl)phosphine oxide (BAPO: 0.5%), and a radical scaven-

ger, 2-hydroxy-4-methoxybenzophenone (HMB: 0.3%) relative to the mass of the polymer. Hydroxyapatite (<200 nm) was added to the mixture with a weight percentage (5%) with respect to all components of the resin except for ethyl acetate in order to represent the final amount within the sample.

Rheology. The complex viscosity of each of the resins was measured at 60 wt% polymer in ethyl acetate with and without 5 wt% HAp nanoparticles (not including the thiol) using a Discovery HR-3 (TA Instrument, DE, USA). The resin (1 mL) was placed on the 25 mm parallel plate geometry with a 0.2 mm gap. The results collected were from a frequency sweep of 0.1 rad s^{-1} to 500 rad s^{-1} at 10% strain at a constant temperature of 25 °C.

3D printing. Tensile bars (ASTM D368 type V), discs (10 mm diameter, 2 mm height), DMA rectangular bars (2 × 3 × 15 mm), and 65% porous gyroid scaffolds were printed from resin with a Carbon (Redwood, CA) M2 printer (λ = 385 nm). Structures were washed post-printing with ethyl acetate, isopropyl alcohol and subsequently submerged in deionized water for post-curing in a B9 Model Cure UV oven (B9Creations, 70 W, 55 Hz, λ = 390–420 nm) for either 5, 15 and 30 minutes. Samples were dried under vacuum at 50 °C and 60 °C for 2, 4, and 6 days for the drying study and subsequently for 8 days for all other experiments.

Micro-computed tomography (micro-CT). The pure PPF and composite printed scaffolds were scanned using micro-CT to reveal their internal structure and to evaluate the distribution of filler within the scaffolds. Micro-CT scans were carried out on a Nikon XTH 225 ST instrument at 140 kV/12 W. Voxel size was typically 8–9 μm. 3D reconstruction of the scans was carried out in the Avizo software (FEI Visualization Sciences Group).

Scanning electron microscopy (SEM). SEM images of the inorganic filler particles and the cut pure PPF and composite 3D printed samples were obtained using an Apreo S SEM (ThermoFisher Scientific) at 2 kV accelerating voltage. All samples were sputtered with a thin Au layer (~5 nm) prior to imaging using a Denton Desk V sputter coater.

Mechanical properties

Tensile testing. Uniaxial tensile tests were conducted using an Instron 5800 Series Universal Testing System (Instron, Norwood, MA). Force and displacement were measured using a 100 N load cell at 10 mm min^{-1} crosshead speed and room temperature (n = 3). The elastic modulus was determined from the slope of the initial linear region, ultimate tensile strength was taken as the maximum of the stress–strain curve, and strain at failure was taken as the final data point before the stress dropped off. A sample size n = 3 was used for all experiments.

Compression testing. Compressive properties of the pure PPF and composite porous gyroid scaffolds (n = 3 for each group) were assessed *via* uniaxial compression testing using a Test Resources 910LX25 servohydraulic test system equipped with a 25 kN load cell. All tests were carried out at a constant displacement rate of 5 mm min^{-1}. The compressive modulus was determined from the slope of the initial linear region of the stress–strain curve (n = 3).

Dynamic mechanical analysis (DMA). Three-point bend measurements (10 mm spacing) were assessed by DMA (TA Instruments RSA G2 Solids Analyzer) using printed rectangular substrates (2 × 3 × 15 mm). A temperature sweep was conducted for n = 3 samples from −50 to 200 °C at a rate of 5 °C min^{-1}, 1 Hz frequency, and 0.01% strain. The storage and loss moduli were plotted as a function of temperature. The glass transition temperature (T_g) was defined as the peak of the tan δ curve from the DMA testing.

Swelling. 3D printed discs were placed in ethyl acetate (15 mL) and allowed to equilibrate for 48 h. The mass of the swollen samples was recorded, and the samples were subsequently dried for 5 days under vacuum. The swelling ratio and sol fraction were calculated using the formula:

$$\text{Swelling ratio} = \frac{W_s - W_d}{W_s},\ \text{sol fraction} = \frac{W_0 - W_d}{W_0}$$

where W_d is the weight of the dried samples, and W_s is the weight of the swollen samples, and W_0 is the initial dry weight of the samples.

JMP analysis. A linear regression model with four degrees of freedom was analyzed using JMP software. The values (n = 3) for mechanical tests and reported for dependent variables were analyzed against the categorical variable of system (which reported either unfilled or composite) and continuous variables of drying time, oven temperature, and post-cure irradiation time (Fig. S17†). The impact of the variable and interactions between variables on the respective dependent variable was evaluated for significance with an effect test. If the value reported for Prob > F is less than 0.05, the null hypothesis is rejected.

Results and discussion

PPF stars with a degree of polymerization (DP_n) of 120 were synthesized according to methods described previously.[5–7] *meso*-Erythritol was utilized as a tetra-functional initiator to produce four-arm PPF stars *via* a ring-opening copolymerization of maleic anhydride and propylene oxide, facilitated by $Mg(BHT)_2(THF)_2$ as a catalyst. The scaled up polymerization (300 g) was conducted at 80 °C in toluene (Fig. S1†) and further isomerized using 0.15 M equivalents of diethylamine at 60 °C in chloroform (Fig. S2†), upon which complete isomerization was determined with ^{1}H NMR by confirming a move from the resonance shift from δ = 6.3 ppm (the *cis*-vinyl proton of the maleate unit) to δ = 6.8 ppm (the *trans*-vinyl proton of the fumarate unit).

Pre-dried polymers were dissolved in ethyl acetate (60 wt% PPF : 40 wt% ethyl acetate) resulting in resins well-below the empirical upper limit viscosity of 10 Pa s required for high resolution printing in CLIP.[26] The viscosity of the resin with and without nanoparticles was determined *via* rheology (Fig. S6†), with the hydroxyapatite nanoparticles increasing the viscosity of the resin by an average of 1.5 Pa s. A radical scavenger and photoinitiator were added to the resins at 0.3 wt% rela-

tive to the mass of the polymer and 0.5% relative to the mass of the polymer, respectively. Previous reports have shown a lack of cytotoxic response with photo-initiated PPF systems.[27] The addition of thiol at a 10 : 1 alkene : thiol molar ratio was completed immediately before printing for each resin. For the nanocomposite resin, HAp nanoparticles were added before the addition of the thiol such that 5 wt% of the final product would contain nanoparticles (all but solvent were considered in this calculation) (Fig. 1). Gyroid triply periodic minimal surface scaffolds (unit cell 6 × 6 × 6 mm, porosity 65%), tensile bars, and DMA bars were 3D printed using both resins and subjected to post curing irradiation (λ = 390–420 nm) for either 5, 15, or 30 min following washing with 2, 4, or 6 days in a vacuum oven at 50 °C or 60 °C, resulting in 36 unique conditions for post-treatment. DMA bars were used to analyze the high and low extremes of the conditions for pure resin and the nanocomposite. Triply periodic gyroid designs were utilized in this study rather than a solid structure since PPF is often used as a bone tissue engineering scaffold material.[28,29] Triply periodic structures are often utilized due to their interconnected pore structure for nutrient transfer and their inherent mean curvature of zero, which is close to the mean curvature of trabecular bone (also close to zero).[30–32] Therefore, evaluating the optimization of these materials within an intended structure served to evaluate their potential as composite scaffolds for regenerative medicine. Samples were examined following printing with SEM and μCT. Aggregates of nanoparticles could be observed in both the SEM and μCT images (Fig. 2A–C) and also confirmed consistent HAp dispersion throughout the scaffolds. The clusters do provide some surface roughness which is helpful for cell adhesion, but too much aggregation would limit the mechanical property augmentation effect and create a non-uniform material. Aggregation is common among nanoparticle fillers in general. van der Waals interactions lead to their aggregation, especially at the nanoscale. Future investigations varying filler type, size, or concentration could warrant the analysis of the zeta potential of the filler systems, which may help with understanding the concentration for repellence. Additives could potentially be added to facilitate better particle dispersion within the resins, but these must be biocompatible.

Tensile measurements were made (n = 3) for each of the scaffold treatment condition at room temperature for both unfilled and composite materials. The modulus, ultimate tensile strength, and strain at failure (Fig. 3A–C) were extrapolated from the stress–strain curves from the slope of the linear region of the curve, the maximum stress of the curve, and the recorded strain before the sample fractured. At 50 °C for the unfilled resin structures, the biggest jump in modulus appeared between 2 and 4 days of drying. However, there was still an increase in properties between 4 and 6 days post-printing. UTS consistently increased with number of drying days and post-cure irradiation time. Intuitively, strain at failure decreases with increasing number of drying days. This trend is similar for the modulus for unfilled resin structures at 60 °C, with the exception that modulus did not increase as much between 4 and 6 days, as the modulus appears to reach a maximum. The UTS also increases but does not tend to increase as drastically between timepoints. Strain at failure remains consistent at 60 °C despite additional time in the vacuum oven.

At 50 °C for the composite conditions, there were consistent increases in modulus as a function of increased drying days. UTS consistently increased with drying days and post-cure irradiation time. Strain at failure also decreases with drying time. This trend follows for the modulus for composite samples at 60 °C; however, the modulus increased more between 4 and 6 days. The UTS also increases more between timepoints than the pure samples. Strain at failure also continues to decrease at 60 °C despite additional time in the vacuum oven.

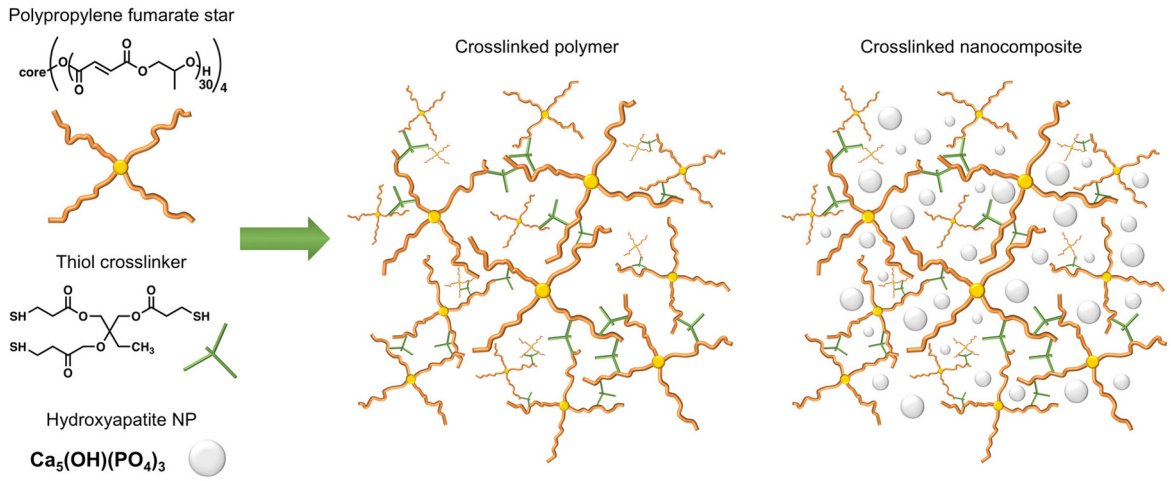

Fig. 1 Poly(propylene fumarate) 4-arm star polymers were crosslinked photochemically using a Carbon M2 printer and a crosslinker with three pendent thiol groups. Hydroxyapatite nanopowder was added to the resin and printed to yield nanocomposites. Tensile bars, DMA bars, and gyroid scaffolds were 3D printed and subjected to different post-curing conditions.

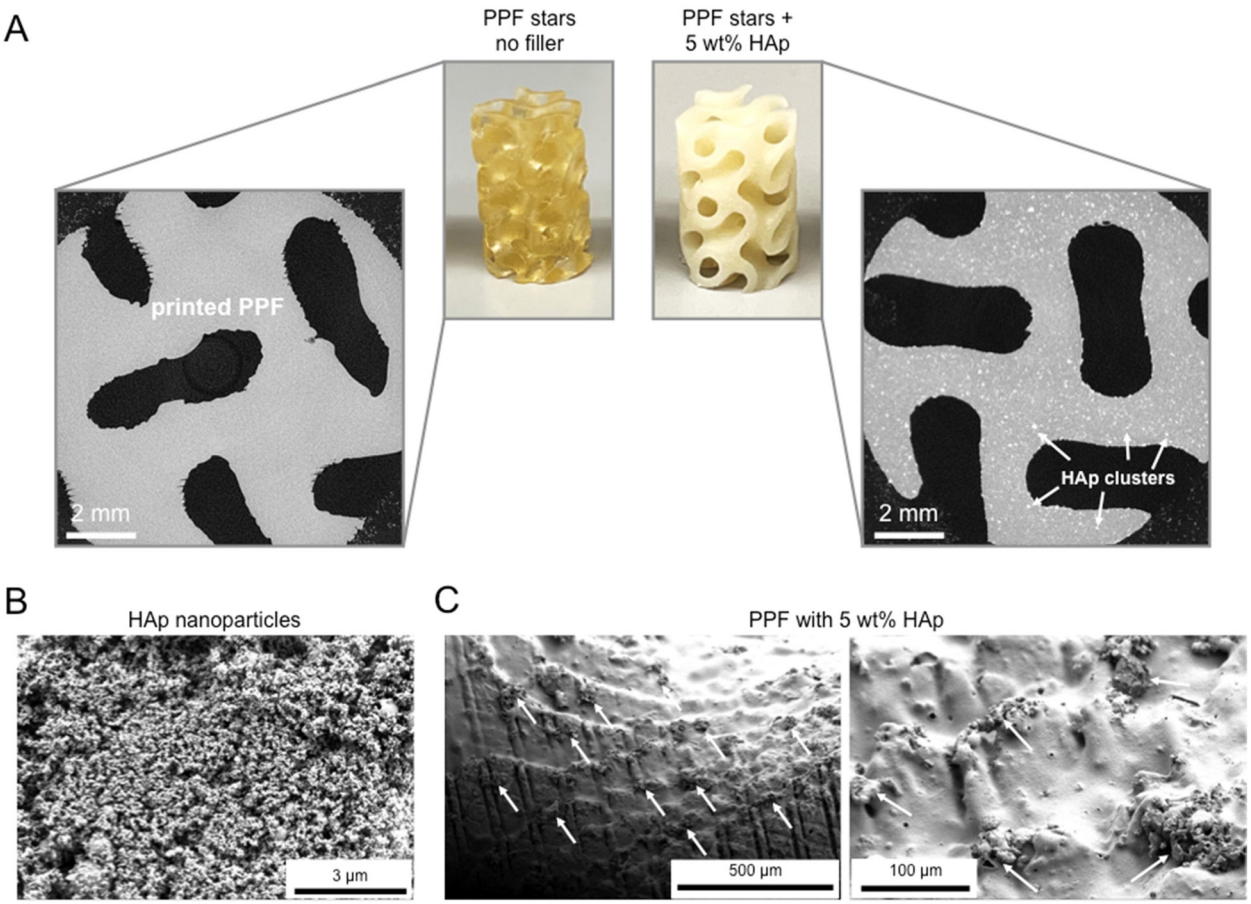

Fig. 2 Each of the printed scaffold materials was evaluated by μCT and SEM in order to observe the microstructure. (A) μCT measurements confirmed the presence of HAp clusters post-printing compared to the pure PPF. (B) HAp nanoparticles were observed with SEM to be uniform. (C) Individual HAp nanoparticles and aggregates were observed on the surface of the printed structures.

A linear regression model with four degrees of freedom was analyzed using JMP software. The values (n = 3) reported for dependent variables of UTS, modulus, and strain at failure were analyzed against the categorical variable of system (which reported either unfilled or composite) and continuous variables of drying time, oven temperature, and post-cure irradiation time (Fig. S17†). The impact of the variable and interactions between variables on the respective dependent variable was evaluated for significance with an effect test. UTS, modulus, and strain at failure were determined to have significant dependence on drying days and temperature. Modulus and strain at failure were also significantly dependent on the system itself. The interaction between the system, the drying time, and drying temperature was observed to be significant in the case of UTS and had some significance for modulus. Further, the interactions between all three continuous variables did have some significant impact on strain at failure. This statistical evaluation supports the observations that temperature and drying time heavily influence the tensile properties.

Compressive properties appeared to follow similar trends with the optimization conditions as tensile properties (Fig. 4A and B). All conditions at 50 °C, samples similarly increase with additional vacuum oven time and post-printing curing time; however, no samples for composites in the 50 °C are capable of outperforming the pure samples for either compressive strength or modulus. This indicates that at 50 °C, the post-processing conditions are still not optimized enough for sufficient curing. At 60 °C, increasing the number of days in the vacuum oven continues to show improvement in material properties; the modulus over doubles from 50 °C to 60 °C. The compressive strength, on the other hand, starts higher at 60 °C but at 6 days, both temperature conditions were comparable. 6 days in the oven is enough time to reach both higher compressive modulus (a difference in average of 40 and 59 MPa higher for the conditions XVI and XVIII, respectively) and compressive strength (a difference in average of 0.09 and 0.39 MPa higher for the XVI and condition XVIII, respectively).

A linear regression model with four degrees of freedom was analyzed using JMP software. The values (n = 3) reported for dependent variables of compressive strength and modulus were also analyzed under the same methods as the tensile behavior (Fig. S17†). Notably, all continuous variables were determined to be significant for both compressive strength and

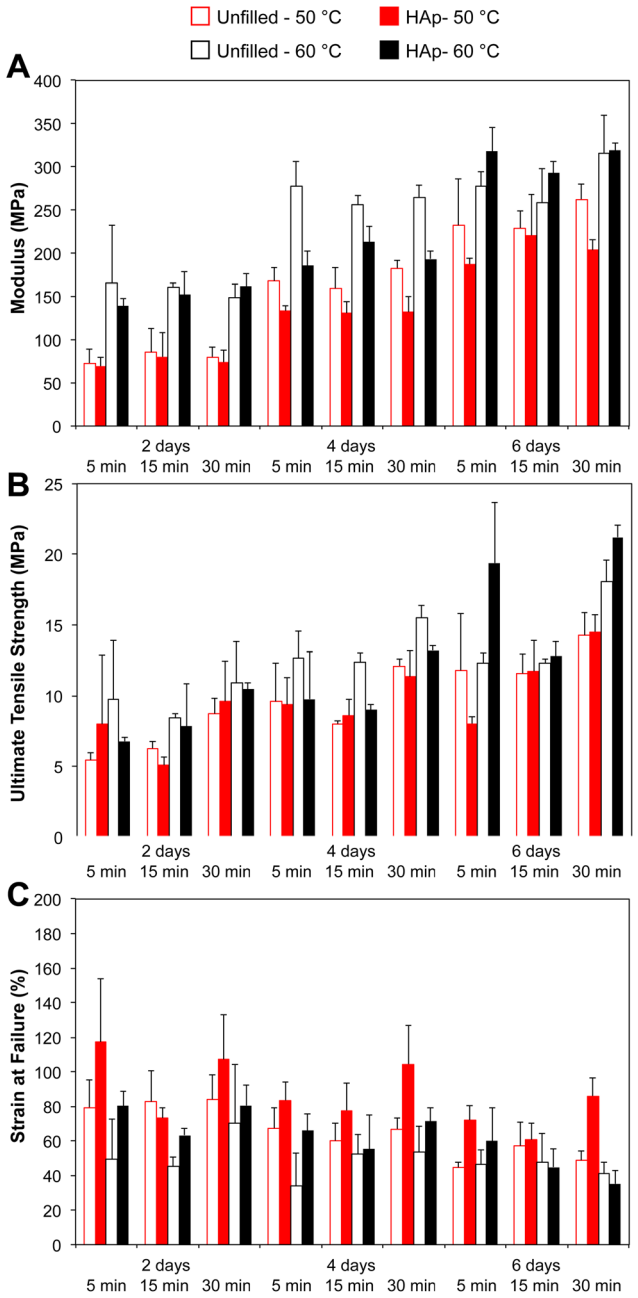

Fig. 3 Tensile properties of the 3D printed PPF stars specimens with and without HAp nanofiller varied depending on the post-printing processing conditions where drying times ranged from 2 to 6 days, and post-cure irradiation time ranged from 5 min to 30 min. Modulus (A) and ultimate tensile strength (B) were heavily and significantly influenced by drying temperature and also drying time. Post-printing irradiation time did not alter mechanical behavior significantly in cases other than UTS. Strain at failure (C) was relatively consistent among unfilled samples and the HAp composite samples.

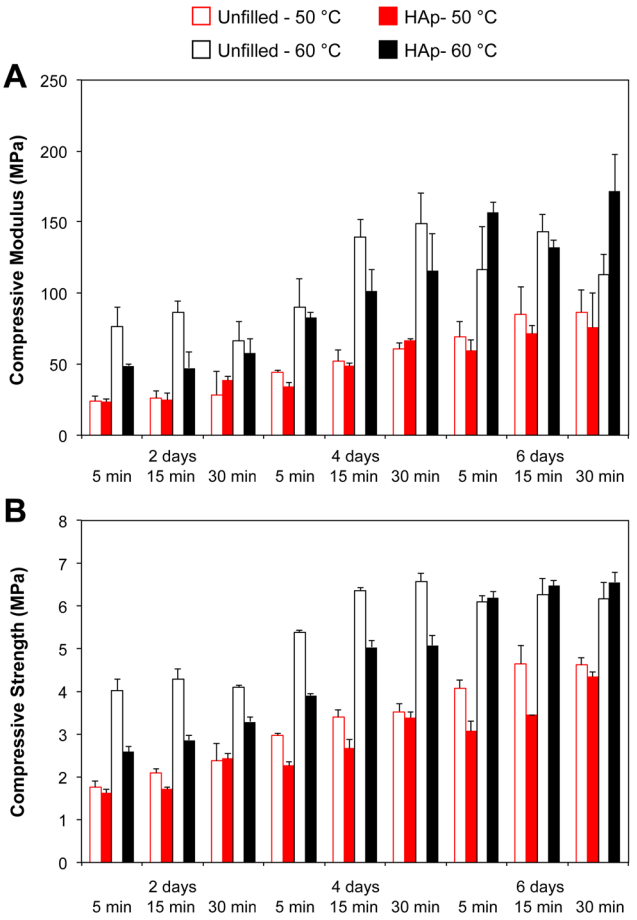

Fig. 4 The compressive strength of 3D-printed, 65% porous triply periodic gyroid scaffolds were measured as a function of post-cure irradiation time, drying temperature, drying duration and presence of HAp nanoparticles. Similar trends in properties were measured as found in the tensile data. Compressive modulus (A) and strength (B) were heavily influenced by drying temperature. After drying for 6 days at 60 °C, the compressive strength and modulus were equal to or enhanced by the nanoparticles. Drying temperature, drying time, and post-cure irradiation were found to significantly affect the compressive strength and modulus.

modulus, with compressive strength also being significantly influenced by the system. Interactions between system, drying days and oven temperature and interactions between drying days and oven temperature were observed to have significant influence on compressive strength and modulus, while only some significance was also observed for both properties with the interactions between system and drying days.

While unfilled printed structures reach a critical saturation point in drying around 4 days, the printed composite samples take longer to reach stable values. This stems from the printing process where the nanoparticles alter the crosslinking effectiveness within the composites, as the light from post-curing and printing is less likely to penetrate through the composite structures with increased opacity of the resin. Thus, the starting point for these scaffolds when entering the drying phase is different from the unfilled scaffolds. As additional crosslinking is present during the drying process, it takes longer for the less-crosslinked composite materials to reach higher crosslink densities and maximized mechanical performance as a result. The tensile study determined that among all changeable post-printing conditions, temperature of the

vacuum makes the most significant effect on the mechanical behavior, followed by time in the vacuum oven and post-curing time. 6 days at 60 °C (XVI–XVIII) is the only condition set where the composite has superior tensile strength and modulus properties over the pure condition. This indicates that at this vacuum oven condition, the post-processing of the composite has likely sufficiently crosslinked and post-cured the samples. The composite samples are stronger in tension than the pure samples only after six days. This along with our previous conclusions allowed to us determine that the condition XVII and XVIII were the most optimized for tensile purposes. The trend follows with the compressive properties explored as well, with conditions XVI and XVIII presenting as the most optimized. The chosen condition shows that to match or maximize the composites to the pure stars in compression properties, XVI and XVIII are most optimal. This concludes that for optimized mechanical behavior the best selection is 30 min of post-curing, followed by 6 days in the vacuum oven at 60 °C.

To date, there has been little investigation on the effects of post-printing processing on 3D-printed materials and composites. However, in the field of filler-reinforced epoxies, post-curing irradiation is considered a standard practice.[33] Liu *et al.* suggest that the addition of fillers can increase curing speed.[34] Singh *et al.* performed a study evaluating temperature of post-curing on these nanocomposite epoxies and observed increasing mechanical behavior with post curing temperatures up until the glass transition temperature of the materials.[35] However, Seretis *et al.* also investigated the time and temperature effects of post-curing irradiation on UTS and strain at break. They concluded that post-cure treatment time affects the performance of the samples more than temperature. Optimum post-printing processing conditions for the system occurred above the respective glass transition temperature of the materials, but for optimum performance, a long drying time will be required.[33] The data obtained in this work follows the latter trends, but also suggests that photochemical systems and composites can be highly variable in terms of optimizing their post-curing conditions.

The DMA analysis of 3D-printed samples in a three-point bending configuration provided further insight into the samples. Unfilled and composite 3D-printed samples for both the minimum and maximum of the post-processing conditions investigated in this work were analyzed. Storage modulus *versus* temperature curves can be observed in Fig. 5. The curves validate similar glassy region, transition region, and rubbery plateau previously observed in this system and other crosslinked networks.[7] Overall, the composite samples exhibit a higher storage modulus at different temperatures (Table 1), which indicated the reinforcement effect that the HAp provides to the polymer matrix.

Both the post-processing conditions end in similar rubbery plateau region among unfilled and composite samples with some increase in rubbery modulus in filled samples. Both unfilled and composite samples at the minimally processed condition exhibit a lower glass transition temperature, indicating ethyl acetate evaporation from the system by the 6th day. The glass transition temperatures are not immensely dissimilar between resin and composite samples subjected to the same post-processing conditions, but the difference in glass transition between the two post-processing condition is almost 20 °C. Further, the onset of the transition region for samples in the maximum condition shifts to higher temperatures as well. This could be the result of an increase in chemical crosslinking as a result of decreased chain mobility and free volume as well as the loss of residual ethyl acetate, although the rubber modulus did not vary between processing treatments as much as between composite and unfilled resin (Table 2).

The nature of the crosslinking at the minimum (I) and maximum (XVIII) post-processing conditions was evaluated by observing the swelling behavior of 3D-printed structures in ethyl acetate (Fig. 6). Due to the ceramic material seized within the polymer matrix, composite samples are less likely to swell

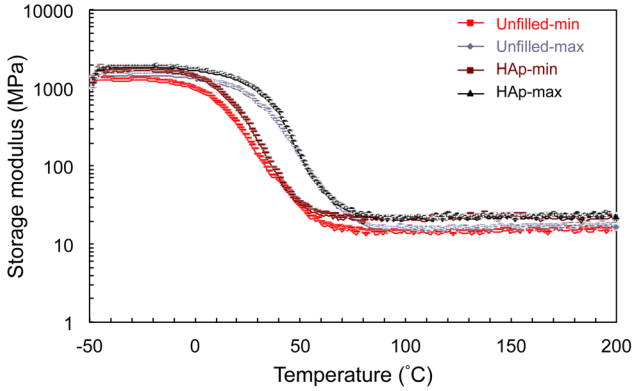

Fig. 5 The DMA curve of storage modulus and temperature demonstrated that the maximum curing condition (XVIII) was more crosslinked in both systems, demonstrated by the increase in the onset of the transition region as well as the glass transition temperature.

Table 1 3D printed samples were post-processed with 18 different condition sets

Condition	Drying days (days)	Temperature (°C)	Post-cure irradiation (min)
I	2	50	5
II	2	50	15
III	2	50	30
IV	2	60	5
V	2	60	15
VI	2	60	30
VII	4	50	5
VIII	4	50	15
IX	4	50	30
X	4	60	5
XI	4	60	15
XII	4	60	30
XIII	6	50	5
XIV	6	50	15
XV	6	50	30
XVI	6	60	5
XVII	6	60	15
XVIII	6	60	30

Table 2 The storage modulus (MPa) was obtained from different temperatures of the curves, ambient temperature (22 °C), physiological temperature (37 °C), and the rubbery plateau region (150 °C)

Drying time	2 days 50 °C		6 days 60 °C	
Irradiation time	5 min		30 min	
Temperature (°C)	Unfilled	Composite	Unfilled	Composite
−25	1290	1680	1470	1840
22	294	474	957	1270
37	70	91	421	594
150	14	23	17	22

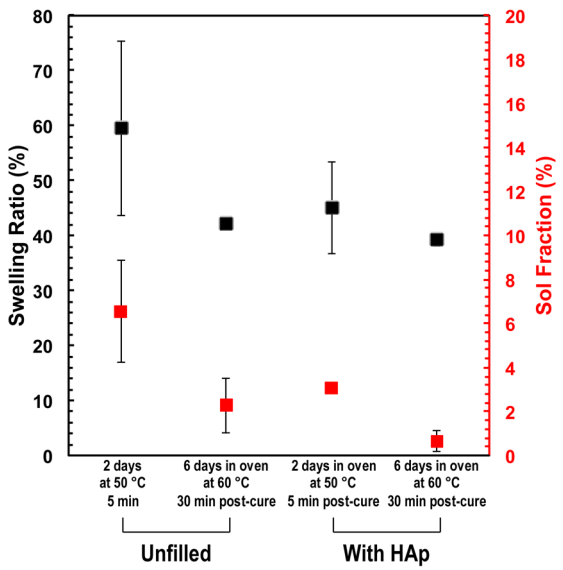

Fig. 6 Swelling ratio and sol fraction of 3D printed unfilled and composite specimens at the minimum and maximum processing conditions.

in solvents. Therefore, composites have a lower swelling ratio than the corresponding unfilled condition. The minimum condition for the pure sample has a higher average swelling ratio than the maximum condition, providing further evidence of additional crosslinking as a result of increased drying time, heat, and post-cure irradiation. The sol fraction of polymer indicated a similar trend to the swelling ratio. The composite sample subjected to the maximum condition exhibited a much smaller sol fraction, also indicating increased crosslinking in the system.

Solely through the modification of post-curing and drying conditions and without changing the underlying chemistry of the system, it was possible to change mechanical behavior from the lowest tensile modulus of 72.9 ± 15.7 MPa to the highest tensile modulus 316.5 ± 43.3 MPa in the unfilled material and 69.4 ± 10.0 MPa to the highest tensile modulus 319.2 ± 8.6 MPa in the nanocomposite material. Compressive behavior could also be modulated from a lowest modulus of 24.3 ± 3.1 MPa to a high of 148.7 ± 21.8 MPa for unfilled materials and a lowest modulus of 23.5 ± 2.4 MPa to a high of 171.7 ± 26.0 MPa for nanocomposite materials. Moreover, the expected reinforcement effect from the HAp was not measurable without appropriately optimized post-processing conditions. The composite systems consistently underperformed the unfilled polymer systems without proper post-processing. The reinforcement effect became apparent when the post-processing conditions were properly tuned. This investigation highlights the need for additional consideration for the post-processing conditions in both unfilled and nanocomposites. Further, this work also highlights the effects of the nanofillers on both printing and post-printing processes.

Conclusions

This study highlights the importance of a systematic investigation and optimization of the post-printing processing conditions of composite structures with and without fillers in order to achieve the best possible composite properties. Longer drying and post-curing irradiation times are necessary for the achievement of maximum mechanical behavior, as well as higher drying temperatures. A filler reinforcement effect can be achieved at longer post-curing times and higher temperatures. This material can be utilized for bone scaffold applications, and there is potential for the investigation of additional fillers and varying filler amounts for a printed construct with tailorable mechanical behavior and other properties.

Conflicts of interest

There are no conflcits to declare.

Acknowledgements

The authors are grateful to Carbon for their continued use of an M2 CLIP printer with an open materials license.

References

1 A. Kirillova, T. R. Yeazel, D. Asheghali, S. R. Petersen, S. Dort, K. Gall and M. L. Becker, *Chem. Rev.*, 2021, **121**, 11238–11304.
2 F. K. Kasper, K. Tanahashi, J. P. Fisher and A. G. Mikos, *Nat. Protoc.*, 2009, **4**, 518–525.
3 X. Xu, A. Awad, P. Robles-Martinez, S. Gaisford, A. Goyanes and A. W. Basit, *J. Controlled Release*, 2021, **329**, 743–757.
4 Z. Cai, Y. Wan, M. L. Becker, Y.-Z. Long and D. Dean, *Biomaterials*, 2019, **208**, 45–71.
5 G. Le Fer, Y. Luo and M. L. Becker, *Polym. Chem.*, 2019, **10**, 4655–4664.
6 G. Le Fer and M. L. Becker, *ACS Appl. Mater. Interfaces*, 2020, **12**, 22444–22452.

7 A. Kirillova, T. R. Yeazel, K. Gall and M. L. Becker, *ACS Appl. Mater. Interfaces*, 2022, **14**, 38436–38447.
8 X. Wang, M. Jiang, Z. Zhou, J. Gou and D. Hui, *Composites, Part B*, 2017, **110**, 442–458.
9 Y.-H. Lee, J. B. Lee, W.-Y. Maeng, Y.-H. Koh and H. E. Kim, *J. Eur. Ceram. Soc.*, 2019, 4358–4365.
10 N. A. Chartrain, C. B. Williams and A. R. Whittington, *Acta Biomater.*, 2018, **74**, 90–111.
11 L. J. Tan, W. Zhu and K. Zhou, *Adv. Funct. Mater.*, 2020, **30**, 2003062.
12 S. Heid and A. R. Boccaccini, *Acta Biomater.*, 2020, **113**, 1–22.
13 H. Zheng, Z. Dai, J. Wei, L. Li, H. Peng, A. Yang, H. Li and G. Lv, *J. Appl. Polym. Sci.*, 2021, **138**, 49751.
14 Y. Gao, G. Zhu, S. Xu, T. Ma and J. Nie, *J. Appl. Polym. Sci.*, 2018, **135**, 45652.
15 Y. Zeng, Y. Yan, H. Yan, C. Liu, P. Li, P. Dong, Y. Zhao and J. Chen, *J. Mater. Sci.*, 2018, **53**, 6291–6301.
16 C. Feng, K. Zhang, R. He, G. Ding, M. Xia, X. Jin and C. Xie, *J. Adv. Ceram.*, 2020, **9**, 360–373.
17 A. Kumar, S. Kargozar, F. Baino and S. S. Han, *Front. Mater.*, 2019, **6**, 313.
18 S.-U. Bae and B.-J. Kim, *Appl. Sci.*, 2021, **11**, 6835.
19 G. Jeong, C. H. Park, B.-Y. Kim, J. Kim, S.-D. Park, H. Yang and W. S. Lee, *ACS Appl. Polym. Mater.*, 2020, **2**, 5228–5237.
20 H. Shi, Z. Zhou, W. Li, Y. Fan, Z. Li and J. Wei, *Crystals*, 2021, **11**, 149.
21 I. K. Cingesar, M.-P. Marković and D. Vrsaljko, *Addit. Manuf.*, 2022, **55**, 102813.
22 E. A. Garcia, C. Ayranci and A. J. Qureshi, *J. Manuf. Mater. Process.*, 2020, **4**, 12.
23 E. Wacławik-Macura and M. Król, *Solid State Phenomena*, 2021, **326**, 51–60.
24 Z. Yang, G. Wu, S. Wang, M. Xu and X. Feng, *J. Polym. Sci., Part B: Polym. Phys.*, 2018, **56**, 935–946.
25 J. A. Wilson, S. A. Hopkins, P. M. Wright and A. P. Dove, *Polym. Chem.*, 2014, **5**, 2691–2694.
26 Y. Luo, G. Le Fer, D. Dean and M. L. Becker, *Biomacromolecules*, 2019, **20**, 1699–1708.
27 M. O. Wang, J. M. Etheridge, J. A. Thompson, C. E. Vorwald, D. Dean and J. P. Fisher, *Biomacromolecules*, 2013, **14**, 1321–1329.
28 K. Nettleton, D. Luong, A. P. Kleinfehn, L. Savariau, C. Premanandan and M. L. Becker, *Adv. Healthcare Mater.*, 2019, **8**, 1900646.
29 E. P. Childers, M. O. Wang, M. L. Becker, J. P. Fisher and D. Dean, *MRS Bull.*, 2015, **40**, 119–126.
30 F. S. L. Bobbert, K. Lietaert, A. A. Eftekhari, B. Pouran, S. M. Ahmadi, H. Weinans and A. A. Zadpoor, *Acta Biomater.*, 2017, **53**, 572–584.
31 J. Shi, L. Zhu, L. Li, Z. Li, J. Yang and X. Wang, *Sci. Rep.*, 2018, **8**, 7395.
32 C. N. Kelly, J. Francovich, S. Julmi, D. Safranski, R. E. Guldberg, H. J. Maier and K. Gall, *Acta Biomater.*, 2019, **94**, 610–626.
33 G. V. Seretis, S. F. Nitodas, P. D. Mimigianni, G. N. Kouzilos, D. E. Manolakos and C. G. Provatidis, *Composites, Part B*, 2018, **140**, 133–138.
34 Y. Liu, Y. Lin, T. Jiao, G. Lu and J. Liu, *Polym. Chem.*, 2019, **10**, 6350–6359.
35 S. K. Singh, A. Kumar and A. Jain, *Plast., Rubber Compos.*, 2021, **50**, 116–126.